Assessing Errors in Variational Dual-Doppler Wind Syntheses of Supercell Thunderstorms Observed by Storm-Scale Mobile Radars

COREY K. POTVIN AND LOUIS J. WICKER

NOAA/National Severe Storms Laboratory, Norman, Oklahoma

ALAN SHAPIRO

School of Meteorology, and Center for Analysis and Prediction of Storms, University of Oklahoma, Norman, Oklahoma

(Manuscript received 26 September 2011, in final form 21 February 2012)

ABSTRACT

Dual-Doppler wind retrieval is an invaluable tool in the study of convective storms. However, the nature of the errors in the retrieved three-dimensional wind estimates and subsequent dynamical analyses is not precisely known, making it difficult to assign confidence to inferred storm behavior. Using an Observing System Simulation Experiment (OSSE) framework, this study characterizes these errors for a supercell thunderstorm observed at close range by two Doppler radars. Synthetic radar observations generated from a high-resolution numerical supercell simulation are input to a three-dimensional variational data assimilation (3DVAR) dual-Doppler wind retrieval technique. The sensitivity of the analyzed kinematics and dynamics to the dual-Doppler retrieval settings, hydrometeor fall speed parameterization errors, and radar cross-beam angle and scanning strategy is examined.

Imposing the commonly adopted assumptions of spatially constant storm motion and intrinsically steady flow produces large errors at higher altitudes. On the other hand, reasonably accurate analyses are obtained at lower and middle levels, even when the majority of the storm lies outside the 30° dual-Doppler lobe. Low-level parcel trajectories initiated around the main updraft and rear-flank downdraft are generally qualitatively accurate, as are time series of circulation computed around material circuits. Omitting upper-level radar observations to reduce volume scan times does not substantially degrade the lower- and middle-level analyses, which implies that shallower scanning strategies should enable an improved retrieval of supercell dynamics. The results suggest that inferences about supercell behavior based on qualitative features in 3DVAR dual-Doppler and subsequent dynamical retrievals may generally be reliable.

1. Introduction

Dual-Doppler wind retrievals are often used to illuminate processes important to convective storm behavior. Kinematic quantities such as deformation and dynamic quantities such as forcing terms in the vertical vorticity equation can be computed from a dual-Doppler wind analysis valid at a single time (e.g., Dowell and Bluestein 2002a; Beck et al. 2006; Wurman et al. 2007). Dual-Doppler analyses valid over a sequence of times (or, if the flow is sufficiently steady-state, at a single time) can be used to compute parcel trajectories. Such analyses have been used to identify source regions of air near a feature of interest (e.g., tornado) and to analyze contributions to the Lagrangian vorticity tendency (e.g., Frame et al. 2009; Marquis et al. 2008; Dowell and Bluestein 2002b; Ziegler et al. 2001; Wakimoto et al. 1998). Calculated parcel trajectories have been combined with thermodynamical retrievals from the dual-Doppler-analyzed winds to examine contributions of vertical forcing terms to updraft and downdraft strength (Cai and Wakimoto 2001; Knupp 1996; Jorgensen and Smull 1993; Lee et al. 1992). As additional high-quality mobile Doppler radar datasets become available from the recent Verification on the Origins of Rotation in Tornadoes Experiment II (VORTEX2) campaign as well as other mobile radar field experiments, dual-Doppler

Corresponding author address: Dr. Corey K. Potvin, National Severe Storms Laboratory, National Weather Center, 120 David L. Boren Blvd., Norman, OK 73072.
E-mail: corey.potvin@noaa.gov

DOI: 10.1175/JTECH-D-11-00177.1

analysis will continue to be regularly used to study storm kinematics and dynamics. A thorough understanding of the characteristics of errors in these analyses is necessary to assess the reliability of inferred storm dynamics.

Dual- and multiple-Doppler (3+ radars) wind retrieval errors have already been systematically examined to varying degrees. For example, the theoretical impacts of Doppler velocity measurement errors on the retrieved wind components have been examined for several dual- and multiple-Doppler analysis methods (Doviak et al. 1976; Ray et al. 1978; Kessinger et al. 1987). Matejka and Bartels (1998) examined the impact of random, bias, and trend errors in the 2D divergence estimates on the analyzed vertical wind for a number of retrieval methods. Given and Ray (1994), Trapp and Doswell (2000), and Majcen et al. (2008) explored the sensitivity of Cartesian analyses to the procedure used to interpolate observations to the analysis grid. Clark et al. [1980 (CHM80)] performed multiple-Doppler analyses of pseudo-observations of a numerically simulated severe multicellular storm and examined the impacts of random observational errors, temporal errors due to advection and evolution of the wind field, and, in the dual-Doppler case, unfavorable cross-beam angles.

As in CHM80, we perform dual-Doppler analyses using radar pseudo-observations generated from a numerically simulated storm. This allows us to systematically vary the observational characteristics and to precisely evaluate analysis errors. Also as in CHM80, we are concerned with the scenario where the radars are sufficiently close to the storm to permit motion scales as small as ~1 km to be partly resolved. This is typical of mobile radar datasets from supercell thunderstorms. However, our investigation differs from that of CHM80 in several important ways. First, we use a more sophisticated storm simulation and radar emulator than were available to that study. Second, we use a numerical supercell thunderstorm as our test case since this storm mode is the subject of a large portion of modern storm-scale dual-Doppler analyses and produces a disproportionate amount of the significant severe weather in the United States. Third, we use a three-dimensional variational data assimilation (3DVAR) dual-Doppler wind retrieval method because of the advantages of this approach over traditional methods (Gao et al. 1999; Potvin et al. 2012a) and in anticipation of its increased usage by the convective storms community. Fourth, we examine a somewhat different subset of dual-Doppler retrieval error sources than did CHM80. Finally, we evaluate errors not just in the dual-Doppler retrievals themselves, but also in vorticity, vorticity tendency, horizontal divergence, and parcel trajectory calculations derived from the dual-Doppler analyses.

The rest of this paper is organized as follows: section 2 describes the generation of the numerical supercell simulation and radar pseudo-observations, the dual-Doppler wind retrieval technique, the parcel trajectory calculations, and the analysis verification. Analysis errors and their sensitivity to important observational characteristics and to the dual-Doppler retrieval settings are examined in section 3. A summary and discussion follow in section 4.

2. Methods

a. Numerical supercell simulation

The supercell was generated using the National Severe Storms Laboratory Collaborative Model for Multiscale Atmospheric Simulation (NCOMMAS; Wicker and Skamarock 2002; Coniglio et al. 2006). The NCOMMAS is a nonhydrostatic, compressible cloud model designed to simulate convective storms in a simplified setting (e.g., flat surface, no surface fluxes or radiative transfer, and horizontally uniform base state). The prognostic variables in NCOMMAS are the wind components u, v, and w, Exner function π, turbulent mixing coefficient K_m, potential temperature θ, water vapor mixing ratio q_v, and hydrometeor mixing ratios.

The supercell simulation proceeded on a stationary 102.4 km × 102.4 km × 20 km domain with 200-m horizontal and vertical spacing. The model was integrated over 2 h using large and small time steps of 2 and 0.25 s, respectively. The sounding (Fig. 1) that provided the model base state is a composite of the wind profile from the 1200 UTC 3 April 1974 Covington, Kentucky, rawinsonde modified to yield a storm motion slow enough to permit the use of a stationary model grid, and a thermodynamic profile similar to that of Weisman and Klemp (1982, 1984) with some modifications to increase the low-level stability below 800 mb to introduce a weak capping inversion more indicative of supercell environments (G. Bryan 2011, personal communication). The supercell thunderstorm was initiated with an ellipsoidal 4-K thermal bubble with horizontal and vertical radii of 10 and 1.4 km, respectively. The microphysical parameterization scheme used in our simulation is a dual-moment version of the Ziegler (1985) scheme (Mansell et al. 2010). The scheme predicts the mixing ratio and number concentration for distributions of cloud droplets, rain, cloud ice crystals, snow, graupel, and hail, as well as the bulk concentration of cloud condensation nuclei and average bulk densities of graupel and hail.

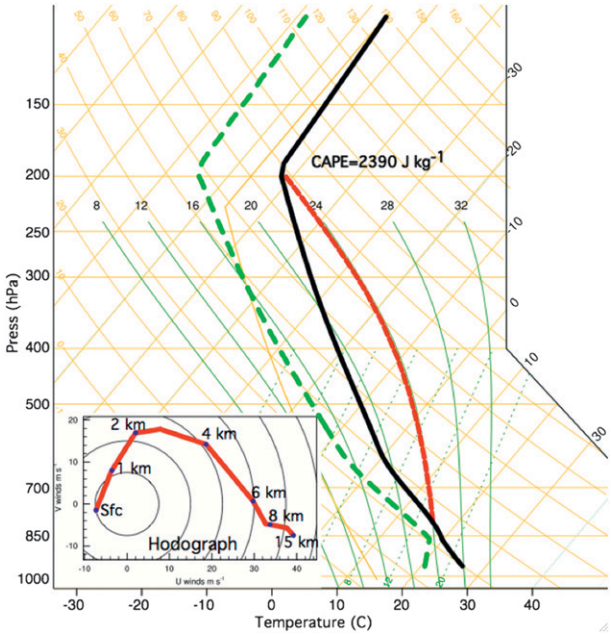

FIG. 1. Sounding used to initialize numerical supercell simulation.

The structure and evolution of the simulated supercell appear reasonably realistic. By 60 min into the simulation, which corresponds to the analysis time of our dual-Doppler retrievals ($t = 0$), the initial storm has fully split, and the right-moving storm (the focus of our analyses) has a well-defined rear-flank downdraft (RFD) whose surface outflow is oriented perpendicular to the gust front (Fig. 2). The maximum surface θ deficit in the cold pool at this time is ~6 K. The gust front and updraft have taken on a horseshoe shape characteristic of observed mature supercells. The storm remains intense through the end of the simulation.

b. Radar emulation

Pseudo-observations of reflectivity Z^{obs} and Doppler velocity V_r^{obs} are generated from the model Z, u, v, and w using a slightly modified version of the Wood et al. (2009) technique to emulate the power-weighted averaging of radial velocities and reflectivities of scatterers within a Gaussian radar beam. Earth curvature and beam refraction are also emulated. The hydrometeor fall speeds used in the calculation of V_r^{obs} are given by $w_t = -2.6Z^{0.107}(1.2/\rho_{\text{sim}})^{0.4}$, where ρ_{sim} (kg m^{-3}) is the height-varying base-state air density in the simulation and Z is given in mm^6 mm^{-3} (Joss and Waldvogel 1970). To emulate the lack of radial velocity data that typically occurs in regions of low signal-to-noise ratio, radial velocity observations are only computed in regions with $Z^{\text{obs}} > 5$ dBZ.

The scanning characteristics of the emulated radars are representative of storm-scale mobile Doppler radars. The radars sample every 150 m in range and 1.0° in azimuth (except 0.5° in one experiment) and have half-power and effective beamwidths of 0.89° and 1.39°, respectively. We use several different volume coverage patterns (VCPs; described later) that represent common scanning strategies used in these deployments. In each case, the radars scan the same elevation angle at the same time, beginning at 0.5° and progressing to steeper tilts. To simulate observational nonsimultaneity, the individual sweeps in each VCP are binned by elevation angle, and blocks of sweeps valid at higher elevation angles are computed from model fields valid at later simulation times. To reduce the storage requirements and to speed up the radar pseudo-observation generation, each block of sweeps is computed from the model data at a single time. To emulate typical measurement errors, random errors having 2 m s^{-1} standard deviation are added to the radial velocity observations.

c. Variational dual-Doppler analysis technique

An overview of the 3DVAR dual-Doppler analysis technique follows; a complete description can be found in Shapiro et al. (2009) and Potvin et al. (2012b), though it should be noted that the vorticity equation constraint adopted in those studies is not imposed in the present work (this constraint did not help in the present case, largely because of the availability of low-level radar data). The technique minimizes the cost function $J = J_O + J_M + J_S$, where J_O, J_M, and J_S are the cost functions associated with the observational, mass conservation, and smoothness constraints, respectively. The relative impacts of the constraints on the analysis are controlled by weighting parameters, denoted below by λ.

The observational cost function

$$J_O \equiv \sum_{\text{Rad1}} \lambda_{O1}(v_{r1}^{\text{obs}} - v_{r1}^{a})^2 + \sum_{\text{Rad2}} \lambda_{O2}(v_{r2}^{\text{obs}} - v_{r2}^{a})^2 \quad (1)$$

sums the root-mean-square (RMS) differences between the observed (v_{r1}^{obs} and v_{r2}^{obs}) and analyzed (v_{r1}^{a} and v_{r2}^{a}) radial winds from two radars, Rad1 and Rad2. To account for the translation of the wind field between the analysis time $t = 0$ (for the Cartesian wind components u^a, v^a, and w^a) and the collection time t^* for the radial wind observation at (x^*, y^*, z^*), the analyzed radial wind at (x^*, y^*, z^*, t^*) is computed from u^a, v^a, and w^a evaluated at

$$(x, y, z) = (x^* - Ut^*, y^* - Vt^*, z^*), \quad (2)$$

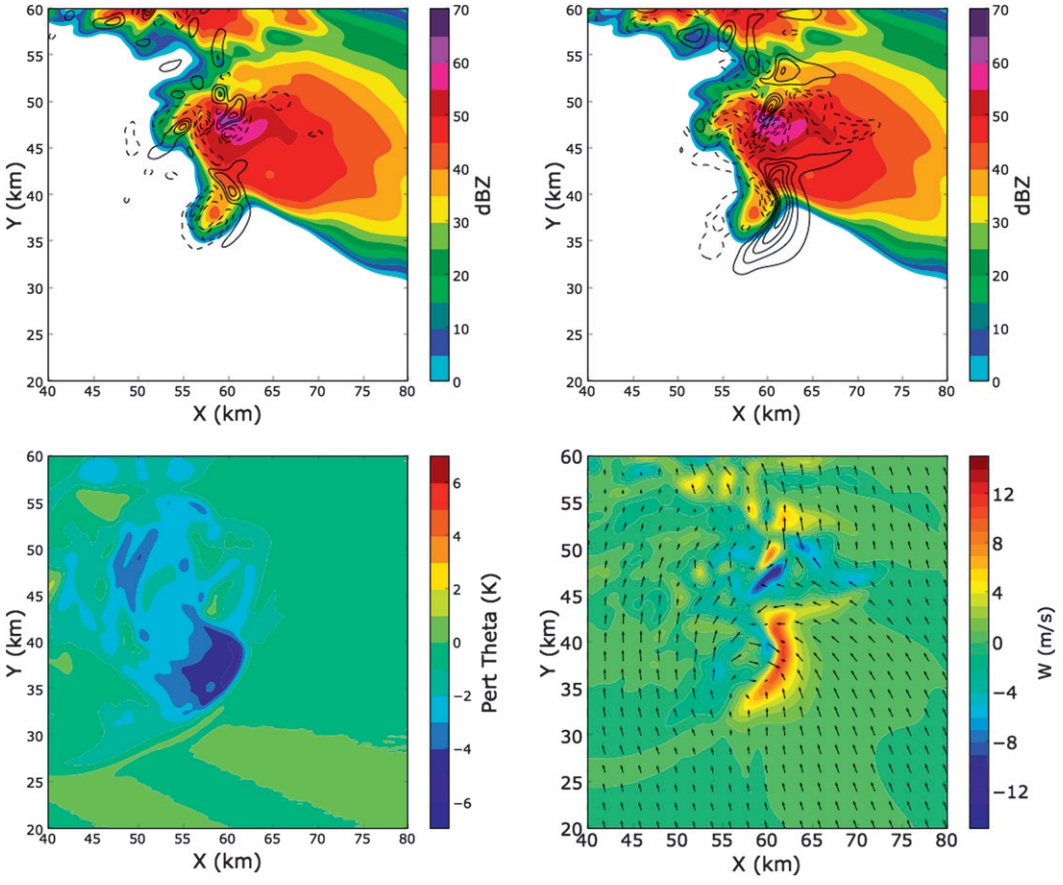

FIG. 2. Filtered model fields valid 60 min into the simulation over the horizontal dual-Doppler analysis domain: (a) dBZ (shading) and vertical vorticity (contoured every 0.005 s^{-1}; dashed lines denote negative values) at $z \approx 1$ km; (b) dBZ (shading) and vertical velocity (contoured every 2 m s^{-1}; dashed lines denote negative values) at $z \approx 1$ km; (c) perturbation potential temperature at $z = 0$; and (d) w (shading) and horizontal wind vectors (arrows) at $z \approx 1$ km. Axes are relative to the southwest corner of the simulation domain.

where U and V are the estimated advection velocity components [i.e., we adopt the frozen-turbulence hypothesis of Taylor (1938)]. In this study, U and V (10 and 0 m s^{-1}, respectively) are treated as constants and were obtained by visually estimating the displacement of the model reflectivity field between two times at several heights. Though more sophisticated advection velocity retrieval methods are available (e.g., Shapiro et al. 2010a,b), we elected to use this simpler approach since it is commonly used in storm-scale dual-Doppler analysis studies (the impact of advection-correction errors will be examined later). The analyzed wind components at (x, y, z) in (2) are obtained using an isotropic 3D Cressman (1959) interpolation method with a cutoff radius R_c (in this study) of 800 m. The suitability of this R_c for our analyses is established in section 3b. The analyzed radial wind for radar n ($n = 1$ or 2) is calculated as

$$v_{r_n}^a = \mathbf{r}_n \cdot [\mathbf{i}u^a + \mathbf{j}v^a + \mathbf{k}(w^a - |w_t|)], \tag{3}$$

where w_t is calculated from the same hydrometeor fall speed formula used in the emulation of v_r^{obs}, and

$$\mathbf{r}_n(x^*, y^*, z^*) = (\cos\theta \sin\phi)\mathbf{i} + (\cos\theta \cos\phi)\mathbf{j} + (\sin\theta)\mathbf{k} \tag{4}$$

is the radial unit vector for the azimuth angle ϕ and elevation angle θ of the radar beam.

The anelastic mass conservation cost function is expressed by

$$J_M \equiv \sum_{\text{Cart}} \lambda_M \left[\frac{\partial u^a}{\partial x} + \frac{\partial v^a}{\partial y} + \frac{\partial w^a}{\partial z} + \frac{w^a}{\rho_s}\frac{\partial \rho_s}{\partial z}\right]^2, \tag{5}$$

where the base-state atmospheric density profile $\rho_s(z)$ is assumed in this study to be $\rho_S(z) = \rho_0 \exp(-z/H)$, with reference density $\rho_o = 1$ kg m^{-3} and scale height $H = 10$ km. The "Cart" label indicates that the summation is performed over the Cartesian analysis grid points.

The smoothness cost function is given by

$$J_S \equiv \sum_{\text{Cart}} \lambda_{S1}\left[\left(\frac{\partial^2 u^a}{\partial x^2}\right)^2 + \left(\frac{\partial^2 u^a}{\partial y^2}\right)^2 + \left(\frac{\partial^2 v^a}{\partial x^2}\right)^2 + \left(\frac{\partial^2 v^a}{\partial y^2}\right)^2\right] + \sum_{\text{Cart}} \lambda_{S2}\left[\left(\frac{\partial^2 u^a}{\partial z^2}\right)^2 + \left(\frac{\partial^2 v^a}{\partial z^2}\right)^2\right] + \sum_{\text{Cart}} \lambda_{S3}\left[\left(\frac{\partial^2 w^a}{\partial x^2}\right)^2 + \left(\frac{\partial^2 w^a}{\partial y^2}\right)^2\right] + \sum_{\text{Cart}} \lambda_{S4}\left(\frac{\partial^2 w^a}{\partial z^2}\right)^2. \quad (6)$$

The smoothness constraint minimizes second-order spatial derivatives in u^a, v^a, and w^a and therefore serves to both dampen small-scale noise and extend analyzed wind gradients into data-sparse regions.

The impermeability condition $\mathbf{V} \cdot \mathbf{n}$ is exactly satisfied along the ground, where $\mathbf{V}$ is the 3D velocity vector and $\mathbf{n}$ is the local unit vector normal to the terrain. Since the lower boundary in our case is flat, this condition reduces to $w = 0$ at $z = 0$. In most of the experiments in this paper, $\lambda_{O1} = \lambda_{O2} = 3$, $\lambda_M = 3$, $\lambda_{S1} = \lambda_{S2} = \lambda_{S3} = 1$, and $\lambda_{S4} = 0.1$. The sensitivity of the analyses to the weighting parameters is explored in section 3c.

The dual-Doppler retrievals proceed over a 40.2 km × 40.2 km horizontal domain centered on the simulated supercell 60 min into the simulation. The height of the dual-Doppler analysis domain varies with the VCP. The same grid spacing, $\Delta = 600$ m, is used in all three dimensions. The characteristics of each VCP are listed in Table 1. Using DEEP, the entire depth of the simulated storm is sampled by the two radars. SHALLOW permits shorter ΔT (potentially advantageous for parcel trajectory computations) at the expense of not sampling higher altitudes of the storm. OVERSAMP uses the same elevation angles as SHALLOW but has $\Delta\phi = 0.5°$, thus trading shorter ΔT for increased azimuthal resolution.

All the dual-Doppler retrievals use data from a single volume scan (data gathered from $t = 0$ to $t = \Delta T$) from each radar and output analyzed fields at a single analysis time. We choose to analyze the wind field at $t = 0$ rather than at some time intermediate between $t = 0$ and $t = \Delta T$ to minimize low-level errors from unaccounted wind field advection and evolution. Though this strategy risks larger errors aloft due to the resultant longer period between the analysis and observation times, it is commonly adopted when the feature(s) of greatest interest (e.g., low-level mesocyclone) occur nearer the ground.

d. Vorticity and parcel trajectory retrievals

Vertical vorticity $\zeta \equiv \partial v/\partial x - \partial u/\partial y$, vertical vorticity tilting $\dot{\zeta}_{\text{tilt}} \equiv -(\partial v/\partial z)(\partial w/\partial x) + (\partial u/\partial z)(\partial w/\partial y)$, vertical vorticity stretching $\dot{\zeta}_{\text{stre}} \equiv -\zeta(\partial u/\partial x + \partial v/\partial y)$, and, in one experiment, horizontal divergence $\delta \equiv \partial u/\partial x + \partial v/\partial y$ are computed from the dual-Doppler-retrieved winds using centered finite differences valid over 2Δ. In section 3h, the fourth-order Runge–Kutta method is used to backward compute parcel trajectories from $t = 60$ min to $t = 45$ min using the model u, v, and w output every 30 s ("true" trajectories) and several series of dual-Doppler analyses valid every $\Delta T + 30$ s (analyzed trajectories).[1] In both cases, the trajectory time step is 1 s. Material circuits C connecting the parcel trajectories at successive times are then computed. Finally, time series of circulation, $\Gamma \equiv \sum_C \mathbf{V} \cdot d\mathbf{l}$, where $d\mathbf{l}$ is the line element vector tangential to C at a given point, are computed around the material circuits.

e. Verification

The verification wind fields are generated from the simulated fields using two steps. First, to match the motion scales in the analyses that can be resolved on the analysis grid, a sixth-order implicit filter (Raymond 1988) is used to strongly damp wavelengths <1.2 km (2Δ) in the 200-m simulated wind fields. Second, to verify the retrievals on the analysis grid points, the verification winds are computed at each analysis point by taking a weighted average of all the filtered verification winds located on and within the (600 m)^3 grid box centered on each analysis point. The verification winds valid on surfaces and edges of the (600 m)^3 grid box are weighted one-half and one-fourth as much, respectively, as winds valid within the 600-m grid box. The verification ζ, $\dot{\zeta}_{\text{tilt}}$, and $\dot{\zeta}_{\text{stre}}$ are computed from the verification u, v, and w using the same finite-differencing stencil as in the analysis procedure.

Verification is performed only within the dual-Doppler domain, defined in this study as the set of analysis points located within 750 m of at least one v_r^{obs}

[1] We performed dual-Doppler analyses every $\Delta T + 30$ s rather than every ΔT to account for the time required for the radar dish to return to its base tilt.

TABLE 1. Volume coverage patterns used in retrievals.

	ΔT (min)	Z_{TOP} (km)	$\Delta\phi$ (°)	Elevation angles θ (°)
DEEP	2.5	13.8	1.0	0.5, 1.5, 2.5, 3.5, 4.5, 6.0, 7.5, 9.0, 10.5, 12.5, 14.5, 16.5, 19.0, 21.5, 24.0, 27.0, 30.0, 33.0
INSTANT	0.0	13.8	1.0	0.5, 1.5, 2.5, 3.5, 4.5, 6.0, 7.5, 9.0, 10.5, 12.5, 14.5, 16.5, 19.0, 21.5, 24.0, 27.0, 30.0, 33.0
SHALLOW	1.5	6.0	1.0	0.5, 1.5, 2.5, 3.5, 4.5, 6.0, 7.5, 9.0, 10.5, 12.5, 14.5, 16.5
OVERSAMP	3.0	6.0	0.5	0.5, 1.5, 2.5, 3.5, 4.5, 6.0, 7.5, 9.0, 10.5, 12.5, 14.5, 16.5

from each radar. All statistics presented herein are computed within horizontal planes of the dual-Doppler domain. To facilitate the interpretation of the RMS error (RMSE) and relative RMSE (RRMSE; RMSE as a percentage of the RMS truth) plots presented below, vertical RMS profiles of the verification (hereafter true) variables are shown in Fig. 3.

3. Results

a. Control experiment

A dual-Doppler retrieval was performed using observations collected by two radars having the sampling characteristics listed in section 2b and using the DEEP VCP (Table 1). The radars were positioned to produce a 60° cross-beam angle (CBA) at the domain center, which is roughly collocated with the storm's hook echo reflectivity signature at 60 min into the simulation (Fig. 4), the time at which all retrievals in this paper are valid. Prior to CTRL, a series of preliminary dual-Doppler retrievals was performed in which the method for interpolating between the observational and analysis grids and the values of the constraint weights λ was varied. The settings that produced the "best" analysis (that which recovered as much of the amplitude of local extrema in the kinematical fields as possible while maintaining acceptably low noise levels) were adopted in CTRL and as the default settings in the remaining retrieval experiments. The sensitivity of the analyses to settings in the dual-Doppler retrieval procedure and to characteristics of the radar observations (CBA and scanning strategy) is explored in subsequent sections. Here, we focus on the analysis errors that occurred in CTRL (Fig. 5).

The RMSE and RRMSE in all six analyzed variables generally increase with height, especially at upper levels of the analysis domain, with the RMSE in all three wind components exceeding 10 m s^{-1} near the domain top. The degradation of the analysis with height is partly attributable to the increasing vertical distance between successive radar scans. The RRMSE in w^a exceeds 40% at all levels above the surface. As expected, smaller relative errors occur in u^a and v^a, however, u^a errors exceed 30% even at some lower levels and v^a errors approach those in w^a at higher levels. Because of spatial discretization errors, relative errors in ζ^a are substantially larger than those in u^a and v^a, and relative errors in δ^a, $\dot{\zeta}^a_{\text{tilt}}$, and $\dot{\zeta}^a_{\text{stre}}$ generally far exceed those in all three wind components. The degradation of the retrieved fields between $z = 0.6$ km and the surface indicates that the 3DVAR framework does not substantially mitigate errors arising from the lack of radar data near the ground. Repeating CTRL using observations with no random errors generally reduced the RRMSEs u^a and v^a by <1 percentage point, RRMSE w^a by <5 percentage points, and RRMSEs δ^a, ζ^a, $\dot{\zeta}^a_{\text{tilt}}$, and $\dot{\zeta}^a_{\text{stre}}$ by <10 percentage points, indicating that most of the analysis errors arose

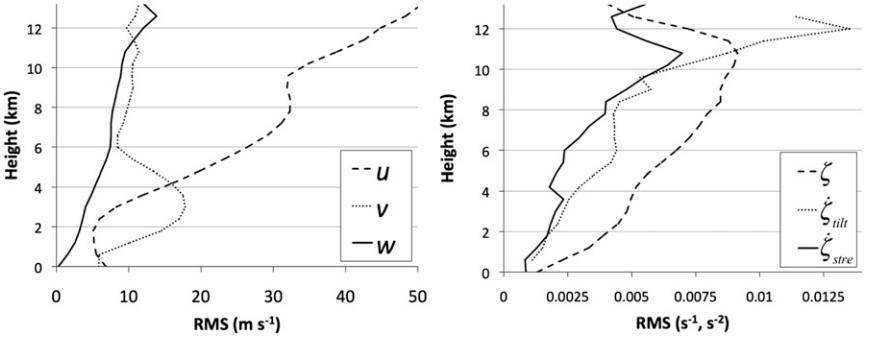

FIG. 3. Vertical RMS profiles of true fields: (left) u (m s^{-1}; dashed line), v (m s^{-1}; dotted line), and w (m s^{-1}; solid line); (right) ζ (s^{-1}; dashed line), $\dot{\zeta}_{\text{tilt}}$ ($\times$100 s^{-2}; dotted line), and $\dot{\zeta}_{\text{stre}}$ ($\times$100 s^{-2}; solid line).

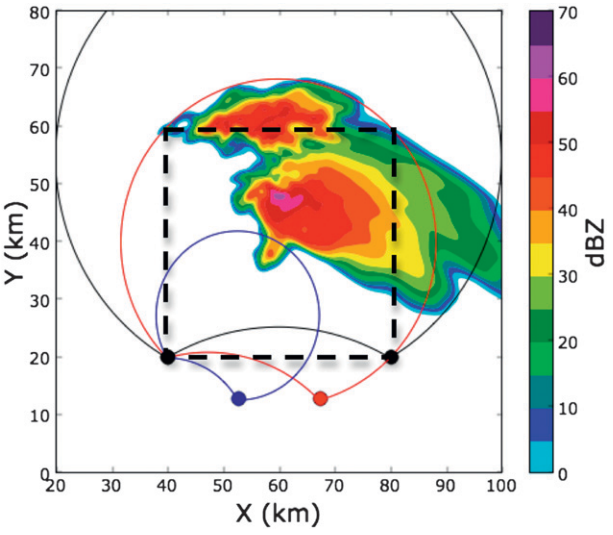

FIG. 4. True Z (shading) and Rad2 locations (dots) for retrievals with CBA = 90° (black), CBA = 60° (red), and CBA = 30° (blue) near analysis domain center. The northern 30° dual-Doppler lobe is depicted in each case. The dual-Doppler analysis domain is outlined by the black dashed square.

from sources other than noisy data (e.g., limitations of the retrieval methodology and of the observational resolution and coverage).

Vertical correlation profiles (Fig. 5d) as well as comparisons of horizontal cross sections of the true and analyzed variables (shown for selected variables and heights in Fig. 6) reveal that much of the RMSE increase with height arises from an increasing mismatch between the true and retrieved wind field patterns. Much of this mismatch at higher levels (see Figs. 6e,f) is due to the retrieved wind field being displaced to the east of the true wind field, indicating that our (constant) estimate for U (10 m s^{-1}) is too small aloft. This motivated a new set of experiments in which U was alternately increased to 12.5, 15.0, 17.5, and 20.0 m s^{-1} (but still held constant over the analysis domain). None of the resulting analyses (not shown) were substantially better than the CTRL analysis, indicating that our use of spatially constant advection correction was too simple for this case. Much of the error at higher levels also appears to result from substantial intrinsic evolution of the flow (for which no provision is made in the retrieval technique) between the analysis time and the times at which upper-level observations are valid. This rapid evolution can be inferred from the large changes in the wind field patterns and local extremum magnitudes between $t = 60$ min and $t = 62$ min (shown at one level for u in Fig. 7).

These results suggest that the analysis errors, especially at higher levels, might have been substantially reduced had more sophisticated methods been used to account for flow advection and intrinsic evolution. Since our primary objective is to examine typical errors in storm-scale 3DVAR dual-Doppler wind syntheses, we did not attempt to use more specialized methods to correct for these processes (e.g., Shapiro et al. 2010a,b; Potvin et al. 2012b). The errors arising from unaccounted wind field advection and evolution in our case are examined in section 3g. From the results already presented we conclude that, given a typical storm-topping mobile radar scanning strategy and method of correcting for flow advection and evolution, caution should be exercised when interpreting 3DVAR dual-Doppler analyses at high altitudes.

b. Sensitivity to interpolation procedure

Studies of traditional dual-Doppler analysis methods have shown that wind retrieval errors can be substantially reduced through the judicious selection of the interpolation scheme used to map the Doppler velocity observations to the Cartesian analysis grid (Given and Ray 1994; Trapp and Doswell 2000; Majcen et al. 2008). Determining the optimal interpolation procedure for a particular problem, however, can be very challenging. For example, using the Cressman method with too large an R_c results in the strong damping of wavelengths that are well-resolved by the observations, whereas using too small an R_c permits the upscale aliasing of minimally resolved wavelengths. The R_c that optimizes the trade-off between these two errors is largely determined by the data spacing, which itself can vary substantially throughout the analysis domain as well as in different dimensions. Irregular data spacing can be addressed using (i) spatially or (ii) directionally varying R_c, but with the caveats that (i) causes the minimal resolvable wavelength to vary by location, making it difficult to distinguish between real and artificial trends in the analysis; and (ii) causes the minimum resolvable wavelength to vary by direction, thus distorting the shape of the input field. Another important consideration is that Doppler velocity moments are themselves the result of a spatiotemporal filtering process over the radar pulse volumes and thus do not produce the same filter response as would point velocity measurements. Finally, it is possible that the behavior of a particular interpolation scheme may be different in our 3DVAR framework than in traditional methods.

Since the optimal interpolation strategy for our problem was not obvious a priori, we performed a series of preliminary retrievals using different interpolation methods and visually and quantitatively examined the analysis errors in each case. The method that produced the best analysis was used in CTRL and all subsequent

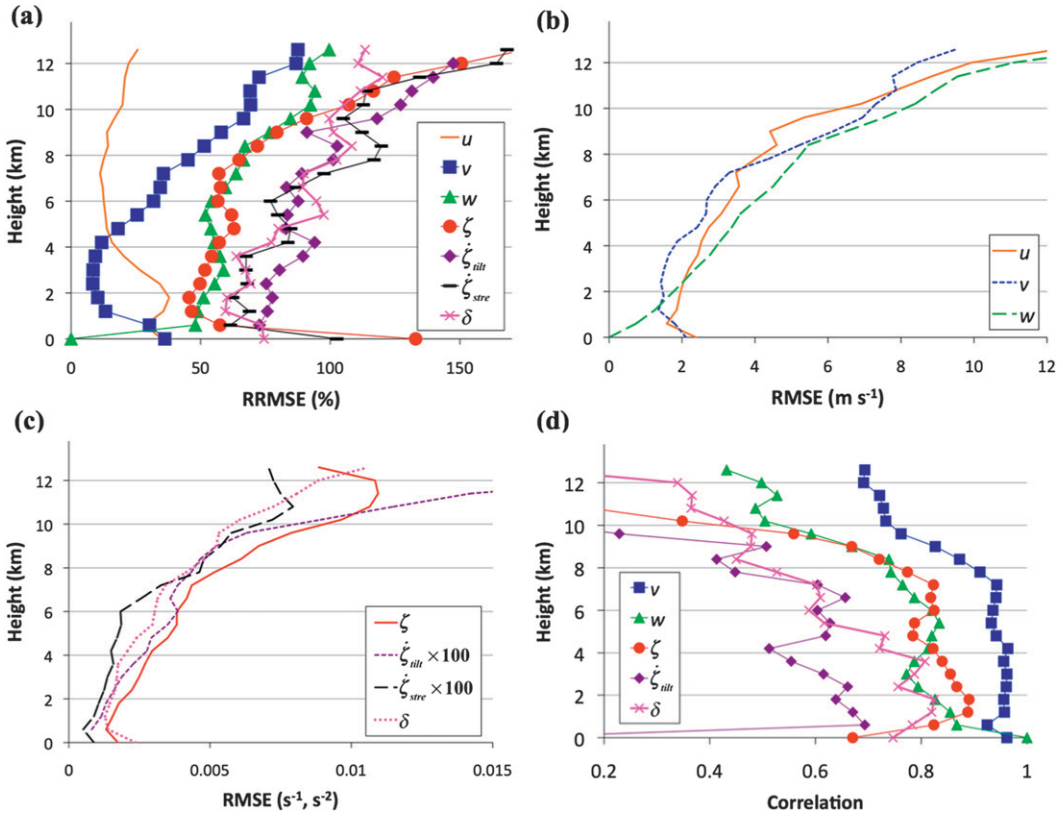

FIG. 5. Errors in CTRL: (a) RRMSE (%) u^a (plain), v^a (squares), w^a (triangles), ζ^a (circles), $\dot{\zeta}^a_{\text{tilt}}$ (diamonds), $\dot{\zeta}^a_{\text{stre}}$ (bars), and δ^a (crosses); (b) RMSE u^a (solid line), v^a (short dashed line), and w^a (long dashed line); (c) RMSE ζ^a (solid line), RMSE δ^a (dotted line), 100 × RMSE $\dot{\zeta}^a_{\text{tilt}}$ (short dashed line), and 100 × RMSE $\dot{\zeta}^a_{\text{stre}}$ (long dashed line); and (d) correlations of true fields with v^a (squares), w^a (triangles), δ^a (crosses), ζ^a (circles), and $\dot{\zeta}^a_{\text{tilt}}$ (diamonds).

experiments. Because the optimal interpolation strategy cannot be so determined in practice, we also examined the sensitivity of the analysis errors to the interpolation method. The first set of retrievals used the one-pass Barnes (1964) scheme.[2] Following Koch et al. (1983), the shape parameter κ was set to $(1.33\Delta)^2$, but with Δ alternately set to a range of values between 200 and 500 m rather than to the mean data spacing as in that study. The second set of retrievals used the one-pass Cressman method with R_c alternately set to a range of values between 600 and 1200 m. The differences in the RMS errors between the best retrievals from each set of experiments were generally <1%, and the analyses were not unduly sensitive to the shape parameter (κ or R_c) in either scheme (results for the Cressman scheme experiments that produced the highest and lowest RMSE are shown in Fig. 8). Thus, we could find no reason to favor one scheme over the other. The Cressman scheme was adopted for all subsequent experiments.

In the third set of interpolation method experiments (not shown), a range-dependent Cressman radius was adopted in which $R_c = ar\sin(\Delta\theta)$, where r is the distance from the radar to the observation; $\Delta\theta$ is the increment between the current and previous elevation angles; and a = 0.5, 1.0, or 1.5. In the final set of tests (also not shown), an anisotropic Cressman weighting function W was used:

[2] The theoretical response function for the two-pass Barnes scheme is sharper than those of both the one-pass Barnes and Cressman methods, and was shown to reduce dual-Doppler retrieval errors in the OSSEs of Majcen et al. (2008). Unfortunately, our implementation of the adjoint for the two-pass Barnes scheme was prohibitively computationally expensive, so we did not examine the impact of using that scheme. However, this does not indicate a fundamental limitation of the 3DVAR approach since (i) the adjoint wall clock time should be considerably reduced by parallelizing the code, and (ii) it may be possible to implement an approximated version of the adjoint that greatly reduces computational cost with minimal loss of accuracy (one or both strategies may be tested in future work). Furthermore, the relative insensitivity of our results to the interpolation method used (see below) suggests that the analysis degradation due to using a one-pass scheme is less in the 3DVAR DDA framework than in traditional methods.

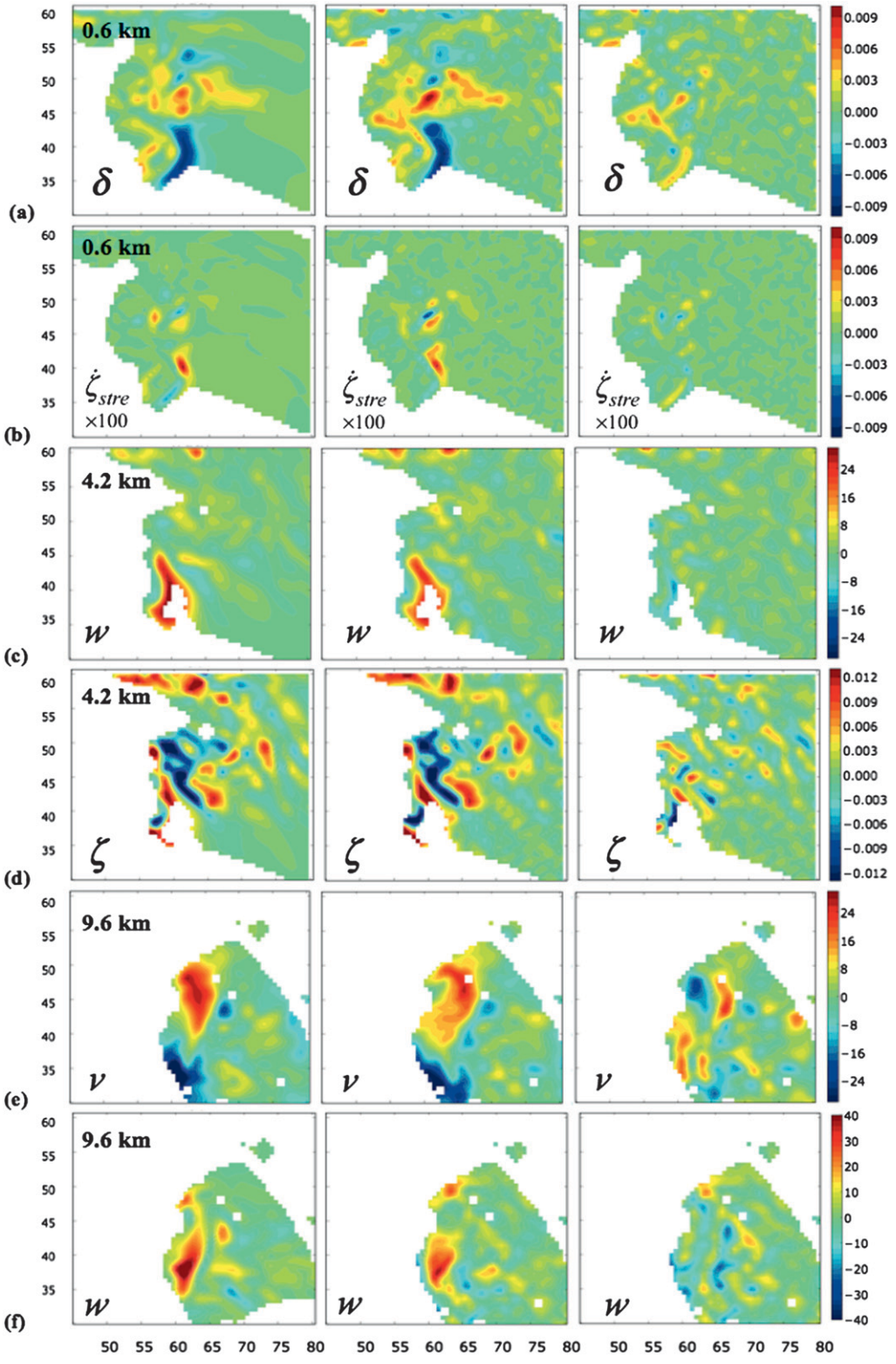

FIG. 6. Horizontal cross sections of (left) true, (middle) analyzed, and (right) analysis errors in (a) δ at z = 0.6 km, (b) $100 \times \dot{\zeta}_{\text{stre}}$ at z = 0.6 km, (c) w at z = 4.2 km, (d) ζ at z = 4.2 km, (e) v at z = 9.6 km, and (f) w at z = 9.6 km. Variables in this and subsequent figures are only plotted where observations from both radars are available within 750 m of the analysis point.

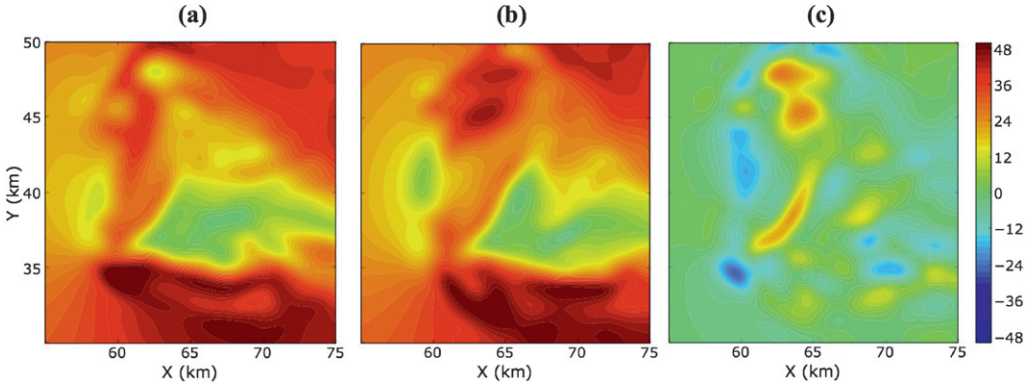

FIG. 7. True u at $z = 8.1$ km: (a) $t = 60$ min, (b) $t = 62$ min, and (c) change in u from $t = 60$ min to $t = 62$ min.

$$W = \frac{(R_c^H)^2 - r_H^2}{(R_c^H)^2 + r_H^2} \times \frac{(R_c^V)^2 - r_V^2}{(R_c^V)^2 + r_V^2}, \tag{7}$$

where the subscripts and superscripts signify horizontal (H) or vertical (V) distances, $R_c^H = ar\sin(\Delta\phi)$ and $R_c^V = ar\sin(\Delta\theta)$, where $a = 0.5$, 1.0, or 1.5. In both sets of experiments, a lower bound of 600 m was set on the cutoff radii to ensure that all observations at least moderately impact the surrounding analysis points. The RMSE generally varied by <10 percentage points among the different retrievals within each of the four experiment sets. The relatively small sensitivity of the analysis to the cutoff radius (or radii) in each experiment set indicates that the trade-off between upscale aliasing of unresolved wavelengths and damping of resolvable wavelengths is not excessively sharp in our problem. This likely largely results from our emulation of the spatial filtering that occurs over the radar probe volume during the velocity moment measurement process. The trade-off is also likely lessened by our use of a least squares approach and of a smoothness constraint, both of which damp aliasing-induced noise. Error differences between the best analyses from each of the four sets of experiments were generally <5% for $\dot{\zeta}^a_{\text{tilt}}$ and $\dot{\zeta}^a_{\text{stre}}$ and <2% for u^a, v^a, w^a, and ζ^a. This suggests that the need to account for spatially and directionally varying data spacing is largely obviated by the correspondingly varying dimensions of the radar pulse volumes over which the velocity moments are valid. Thus, a constant R_c (800 m) was adopted for all subsequent experiments.

c. Sensitivity to constraint weighting parameters

The relative impact of each constraint on the analysis is conveniently controlled through the weighting parameters λ. In previous tests of our dual-Doppler retrieval algorithm (Shapiro et al. 2009), the u^a, v^a, and w^a were relatively insensitive to λ_M and only moderately sensitive to λ_O and λ_S. To confirm that this was the case here and to determine whether greater sensitivity occurred in the vorticity and vorticity tendency variables, we performed a set of experiments in which each of the λ were individually varied.

All the analyzed variables were roughly as sensitive to λ_S as to λ_O. Analyses of all the variables were substantially less sensitive to λ_M than to the other two parameters. As a result, increasing λ_S by a given factor had roughly the same effect on the analysis as decreasing λ_O by the same factor, and vice versa. All of these results are consistent with Shapiro et al. (2009).

The sensitivity of w^a and $\dot{\zeta}^a_{\text{stre}}$ to λ_S is shown in Fig. 9. The sensitivity of u^a and v^a was similar to that of w^a, and the sensitivity of ζ^a and $\dot{\zeta}^a_{\text{tilt}}$ was intermediate between that of w^a and $\dot{\zeta}^a_{\text{stre}}$. Fortunately, the RMSE u^a, v^a, and w^a did not vary significantly among the experiments. However, substantial differences occurred in ζ^a, $\dot{\zeta}^a_{\text{tilt}}$, and $\dot{\zeta}^a_{\text{stre}}$ at most analysis levels. Inspection of horizontal cross sections of the retrieved fields (not shown)

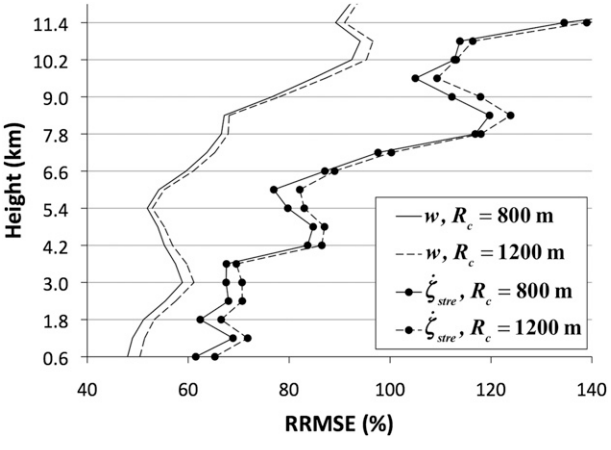

FIG. 8. RRMSE (%) w^a (plain lines) and $\dot{\zeta}^a_{\text{stre}}$ (circles) for retrievals using constant $R_c = 800$ m (solid lines) and 1200 m (dashed lines).

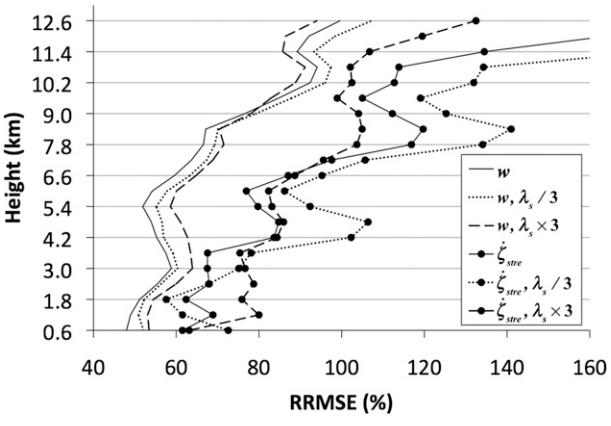

FIG. 9. RRMSE (%) w^a (plain lines) and $\dot{\zeta}^a_{\text{stre}}$ (circles) for CTRL (solid lines) and retrievals using $\lambda_S/3$ (dotted lines) and $\lambda_S \times 3$ (dashed lines).

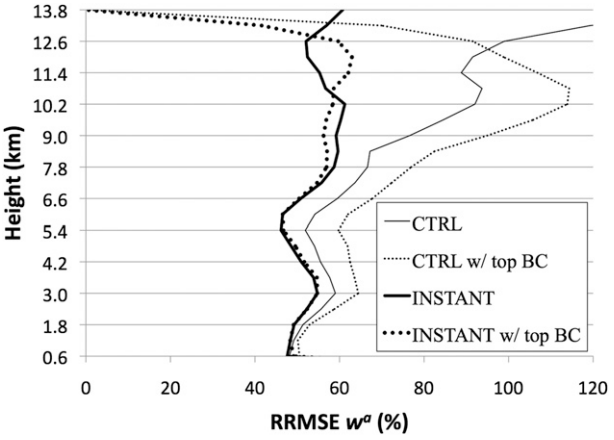

FIG. 10. RRMSE (%) w^a for CTRL (solid line), INSTANT (thick solid line), CTRL with w^a fixed at truth at analysis domain top (dotted line), and INSTANT with w^a fixed at truth at analysis domain top (thick dotted line).

revealed that the differences were primarily in the magnitudes, not the patterns, of the retrieved fields, an expected effect of our varying the level of smoothing in the analysis. The substantial sensitivity of ζ^a, $\dot{\zeta}^a_{\text{tilt}}$, and $\dot{\zeta}^a_{\text{stre}}$ to the relative weight of the smoothness constraint indicates that λ_S should be chosen carefully if quantities involving spatial derivatives of the retrieved wind components are to be computed. This problem is not unique to the 3DVAR approach; spatial filtering is also required in traditional dual-Doppler retrievals when high-amplitude noise would otherwise arise in the analysis.

d. Impact of an upper-level boundary condition

When radar observations are available through the depth of the storm, analysts that use traditional dual-Doppler retrieval techniques often impose an upper-level boundary condition on w^a in addition to the lower-level impermeability condition (e.g., O'Brien 1970; Ray et al. 1980). This approach is primarily intended to mitigate the compounding errors that occur during the upward integration of the 2D divergence estimates. Because divergence is not explicitly integrated in our 3DVAR technique, this type of error is avoided in our analyses. Nevertheless, to determine whether imposing a second, upper-level boundary condition on w^a could reduce the large upper-level errors in our analysis, we repeated CTRL with w^a fixed at the true w at the domain top. The perfect boundary condition improved w^a over the top three analysis levels but degraded w^a at all other levels (Fig. 10). When the experiment was repeated using an instantaneous VCP (INSTANT; Table 1), the top boundary condition did not generally degrade w^a, nor did it generally improve it. The impact of the top boundary condition on u^a and v^a was negligible in both experiments. The limited ability of the mass conservation and smoothness constraints to communicate information about w^a downward from the top boundary likely resulted in part from the solution being underdetermined near the domain top because of the sparseness of the data. The degradation of the CTRL analysis may not be surprising given the particularly large errors in the CTRL δ^a and, thus, $\partial w^a/\partial z$, near the top of the analysis domain due to unaccounted flow advection and evolution. Because fixing w^a to truth at the top of the domain failed to improve upon the CTRL analysis, no further attempts were made to impose an upper-level boundary condition on w^a.

e. Impact of cross-beam angle

Owing to the many difficulties inherent in mobile radar storm intercepts (e.g., radar siting, road network limitations, and rapid and/or variable storm motion), CBAs are often very suboptimal (i.e., much less than 90°). To explore the sensitivity of the analyses to the CBA, CTRL was performed with Rad2 successively repositioned to effect CBAs at the analysis domain center of ~90° or ~30° (CBA90 and CBA30, respectively). The distances of the radars to the center of the domain remained the same as in CTRL. The relocated Rad2 positions are shown in Fig. 4.

As with CTRL, a series of preliminary experiments was performed to optimize the constraint weighting parameters. As the CBA was decreased, the wind analysis became less constrained by the radial wind observations, requiring that the λ_S be decreased to avoid oversmoothing the analyzed fields. In CBA90, $\lambda_{S1} = \lambda_{S2} = \lambda_{S3} = 3$ and $\lambda_{S4} = 0.3$; in CBA30, $\lambda_{S1} = \lambda_{S2} = \lambda_{S3} = 0.3$ and $\lambda_{S4} = 0.01$.

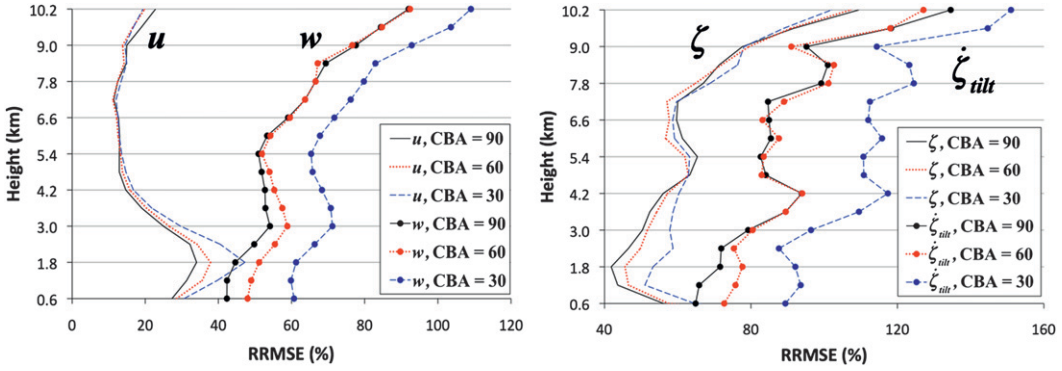

FIG. 11. RRMSE (%) for retrievals with CBA = 90° (CTRL; solid lines) and Rad2 relocated to produce CBA = 60° (short dashed lines) and CBA = 30° (long dashed lines): (left) u^a (plain lines) and w^a (circles); (right) ζ^a (plain lines) and $\dot{\zeta}^a_{\text{tilt}}$ (circles).

Increasing the CBA from 60° to 90° did not substantially improve the analysis (Fig. 11). Decreasing the CBA from 60° to 30° had a larger (detrimental) impact on the RMSE, but the CBA30 fields were still reasonably accurate (Fig. 12). These results are encouraging given the difficulty of realizing large CBAs in mobile radar deployments. The impact of small CBAs on parcel trajectory calculations is examined in section 3h.

f. Impact of fall speed errors

Dual-Doppler retrievals using observations from shallow-scanning radars are generally insensitive to errors in the parameterized hydrometeor fall speeds since the vertical particle velocity projects only weakly in the radial direction. When observations are used from a pair of deep-scanning radars, however, errors in w_t will have a greater impact on the analysis. To characterize this impact, a set of retrievals using DEEP observations was performed with various types of error (Table 2) added to the (perfect) w_t calculated by the technique. The RMSE in all variables increased by <2 percentage points at all heights. Since the nature of w_t errors in practice is not well known, we cannot draw any firm conclusions from these results. However, these experiments do demonstrate that the analyses are resilient to a range of error modes in w_t, which suggests that real-world analyses may not be severely contaminated by imperfect fall speed parameterizations. This result is particularly encouraging for higher-frequency (e.g., X band) radars, which can suffer severe attenuation and thus dramatically underestimate w_t.

g. Impact of scanning strategy

One common alternative to using a deep-scanning strategy is to sample only the lower/middle levels of the storm. This reduces ΔT and, thus, the interval between successive dual-Doppler analyses (the impact of shorter ΔT on parcel trajectory calculations is examined in section 3h). To explore the impact of omitting upper-level radar observations on the analysis, we performed a retrieval experiment using the SHALLOW VCP (Table 1) with Z_{TOP} = 6.0 km (Fig. 13). Fortunately, excluding upper-level observations did not substantially degrade the analysis at lower levels. Repeating the SHALLOW retrieval with an azimuthal increment of 0.5° and thus twice as large a ΔT (i.e., OVERSAMP) increased the RMSE at all levels. Some kinematical features were better resolved using the OVERSAMP VCP because of the enhanced spatial resolution (not shown). However, errors from flow unsteadiness grew because of the longer periods between the analysis and observation times relative to the retrievals with DEEP and SHALLOW, resulting in a net RMSE increase. This result highlights the importance of considering the trade-offs between spatial resolution and volume scan time when designing scanning strategies.

To examine the impact of wind field unsteadiness errors on our analyses, CTRL was repeated using an instantaneous version (ΔT = 0) of DEEP (INSTANT). The resulting error reduction, particularly at higher analysis levels, was very large (Fig. 13). Evidently, the limited ability of our simple advection-correction method to account for the complex evolution of the wind field between the analysis and observation times, particularly at higher levels, was a major source of error in our analyses. It is possible that these errors could be substantially reduced through a more sophisticated advection-correction method (e.g., the spatially variable technique of Shapiro et al. 2010a,b). However, visual inspection of the model wind fields at successive times suggested that much of the wind field unsteadiness arises from intrinsic evolution, not just advection, of the wind field (section 3a). Accurately accounting for evolution of complex flows can be very challenging (e.g., Potvin

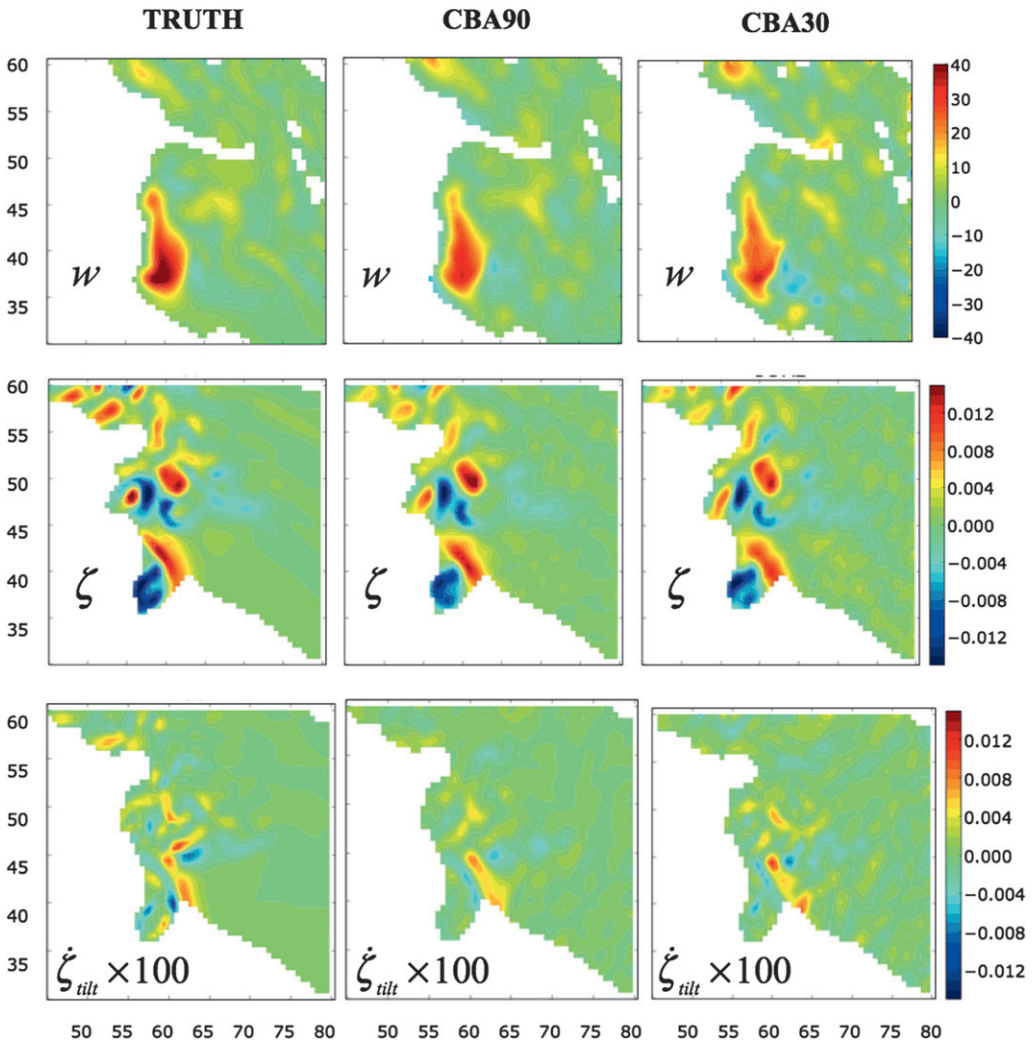

FIG. 12. Horizontal cross sections of (left) true fields, and fields retrieved using (middle) CBA = 90° and (right) CBA = 30°: (top) w at $z = 6.0$ km; (middle) ζ at $z = 1.8$ km; and (bottom) $\dot{\zeta}_{tilt} \times 100$ at $z = 1.8$ km. The 20°, 30°, and 40° dual-Doppler lobes for CBA30 are plotted in black.

et al. 2012b). Thus, using rapidly scanning radars may be the more effective strategy for reducing errors due to wind field unsteadiness. In the absence of rapid-scan data, it is strongly recommended that dual-Doppler retrievals of upper-level winds in supercells use advanced methods to account for flow unsteadiness.

h. Parcel trajectories

To explore the potential impacts of some of the retrieval errors examined above on the interpretation of supercell dynamics, 1000 sets of parcel trajectories were initiated around a 3-km-radius ring (sized to circumscribe most of the low-level circulation within the potentially tornadic region of the storm) roughly centered on the ζ maximum at $z = 1.2$ km. Each set of trajectories was computed backward in time using the model winds or the CTRL (section 3a), SHALLOW (section 3g), or CBA30 (section 3e) wind analyses. Horizontal and x–z projections of the material circuits connecting the trajectories at $t = 57$ min and $t = 50$ min (3 and 10 min

TABLE 2. Errors added to w_t in retrievals presented in section 3f.

Bias	Random error (σ)
0	5 m s^{-1}
0	10 m s^{-1}
5 m s^{-1}	5 m s^{-1}
−5 m s^{-1}	5 m s^{-1}
−50%	0
+50%	0
0	50%
−50%	50%
+50%	50%

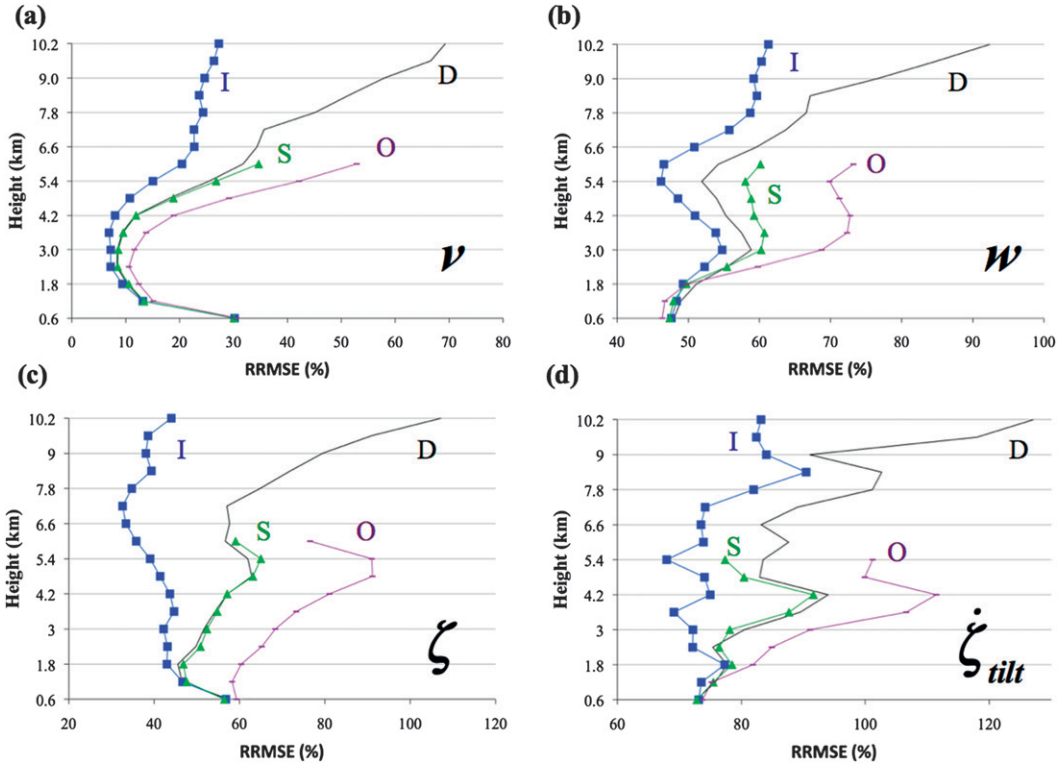

FIG. 13. RRMSE (%) for DEEP (plain lines), SHALLOW (triangles), OVERSAMP (violet lines), and INSTANT (squares): (a) v^a, (b) w^a, (c) ζ^a, and (d) $\dot{\zeta}^a_{\text{tilt}}$. Letters next to the curves represent their corresponding VCPs.

prior to the dual-Doppler analysis time, respectively) are shown in Figs. 14a,b. Encouragingly, all three dual-Doppler analyses permitted qualitatively accurate diagnoses of the source regions of air in the potentially tornadic region of the storm. The timing of the rapid increase of circulation experienced by the circuit after $t = 55$ min was also well-retrieved in all three experiments (Fig. 14c). However, the substantial underestimation of circulation at earlier times, and consequent overestimation of the increase in circulation prior to $t = 55$ min, would imply (via the Bjerknes circulation theorem) a much larger baroclinic contribution to circulation ($\sim 7 \times 10^5$ m^2 s^{-1}) than actually occurred during this period ($\sim 5 \times 10^5$ m^2 s^{-1}). The underestimation of circulation in the forward flank and the magnitudes of the circulation errors are consistent with a similar analysis of synthesized Doppler on Wheels (Wurman et al. 1997) radar observations of a simulated supercell (Markowski et al. 2012).

The smaller ΔT in SHALLOW enabled a more accurate retrieval of parcel trajectories in regions of strongly curved flow, and improved the circulation analysis after $t \approx 57$ min. These results suggest that shallower scanning strategies will benefit investigations of low-level supercell dynamics. Fortunately, the parcel trajectory errors were only moderately larger in CBA30 than in CTRL, and the circulation analysis was roughly as good in both cases. This suggests that quasi-optimal CBAs will not always be required for useful dynamical information to be inferred from low-level supercell wind analyses. That the parcel trajectory and circulation analyses were not substantially degraded by using the less optimal CBA or scanning strategy is encouraging. However, caution should be exercised in extending these results to supercells containing a strong tornado or other vortex, in which case the sensitivity of these analyses to dual-Doppler wind retrieval errors may increase substantially, especially if a smaller radius is chosen for the initial circuit.

4. Summary and discussion

Given the ubiquity and scientific value of dual-Doppler wind retrievals in studies of supercell thunderstorms, improved knowledge of the errors characteristic of these and subsequent dynamical retrievals should facilitate progress in understanding supercell behavior. The Observing System Simulation Experiment (OSSE) framework adopted for this study permitted precise evaluation of these errors and their sensitivity to a number of recognized dual-Doppler retrieval error sources. We chose to emulate close-range mobile radar

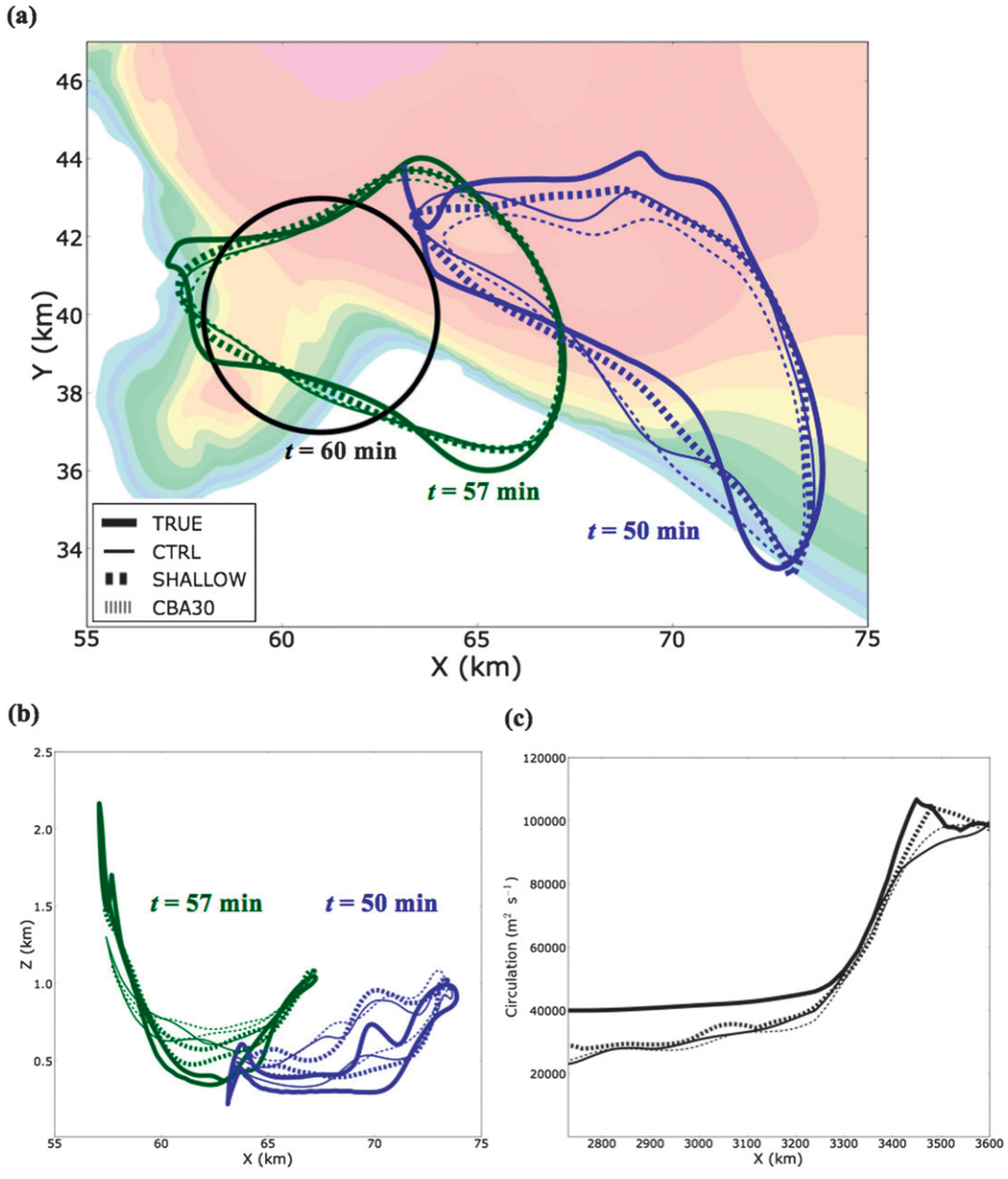

FIG. 14. (a) Horizontal projections of material circuits valid at $t = 57$ min (green curves) and $t = 50$ min (blue curves) for parcel trajectories initiated around 3-km-radius ring (black circle) at $t = 60$ min, $z = 1.2$ km. The trajectories were computed from the true (thick solid lines), CTRL (thin solid lines), SHALLOW (thick dashed lines), and CBA30 (thin dashed lines) wind fields. The model dBZ valid at $z = 1.2$ km, $t = 60$ min (shading) is displayed in the background. (b) Vertical (x–z) projections of the true, CTRL, and SHALLOW circuits. (c) Time series of circulation computed around the circuits.

datasets in our experiments since they are increasingly common and, owing to their relatively high spatiotemporal resolution, have enhanced potential to illuminate supercell kinematics and dynamics.

Many of the results were encouraging with regard to analysis errors. Similar wind and vorticity analyses were obtained using two of the most popular interpolation methods (Barnes or Cressman), and the results were not unduly sensitive to the specification of the shape parameter or influence radius. Additionally, the analyses were not very sensitive to errors in the estimated hydrometeor fall speeds nor to the omission of upper-level radar observations. The latter result suggests that confining volume coverage patterns to the region of interest may be a viable strategy for reducing volume scan times, at least when a 3DVAR dual-Doppler retrieval method

(which obviates the need to scan near storm top to impose an upper-level boundary condition on vertical velocity) is used. Finally, low-level parcel trajectories initiated near the main updraft and RFD were qualitatively accurate, as were time series of circulation along the computed material circuits.

On the other hand, significant errors arose from several sources in the analyses. The magnitudes of local extrema in the retrieved vorticity and vorticity tendency fields were sensitive to the relative weight of the smoothness constraint in the analysis. This problem is not unique to the 3DVAR approach; spatial filtering is also required in traditional dual-Doppler retrievals when high-amplitude noise would otherwise arise in the analysis. The assumptions of spatially constant storm motion and zero storm-relative flow evolution led to significant errors in the analyzed wind field position and pattern at the middle and upper levels. In addition, improved spatial resolution of the wind fields due to azimuthal oversampling was countered by increased flow unsteadiness errors due to longer periods between the analysis and observation times. These results highlight the importance of considering the trade-off between spatial and temporal resolution when designing scanning strategies. To the extent that the translation and evolution of real supercell wind fields are as rapid and complex as that in our simulation, it would likely be very difficult to accurately account for flow unsteadiness in the dual-Doppler analyses.

The locally large errors in the retrieved horizontal divergence, vorticity, and vorticity tendency fields and in the circulation analyses imply that hypotheses relying heavily upon the quantitative accuracy of such variables should be viewed with caution. This is especially true very near the ground, where a lack of Doppler velocity observations can result in severe analysis errors even in the 3DVAR framework. On the other hand, the results also suggest that inferences about supercell behavior based on qualitative features in 3DVAR storm-scale dual-Doppler wind syntheses and subsequent dynamical retrievals may generally be reliable.

Acknowledgments. The first author was supported by a National Research Council Research Associateship Award at the NOAA/National Severe Storms Laboratory. We thank Conrad Ziegler for his helpful review of a preliminary draft of this manuscript. We are also grateful to Yvette Richardson and two anonymous reviewers for their help in further improving the paper.

REFERENCES

Barnes, S. L., 1964: A technique for maximizing details in numerical weather map analysis. *J. Appl. Meteor.,* **3,** 396–409.

Beck, J. R., J. L. Schroeder, and J. M. Wurman, 2006: High-resolution dual-Doppler analyses of the 29 May 2001 Kress, Texas, cyclic supercell. *Mon. Wea. Rev.,* **134,** 3125–3148.

Cai, H., and R. M. Wakimoto, 2001: Retrieved pressure field and its influence on the propagation of a supercell thunderstorm. *Mon. Wea. Rev.,* **129,** 2695–2713.

Clark, T. L., F. I. Harris, and C. G. Mohr, 1980: Errors in wind fields derived from multiple-Doppler radars: Random errors and temporal errors associated with advection and evolution. *J. Appl. Meteor.,* **19,** 1273–1284.

Coniglio, M. C., D. J. Stensrud, and L. J. Wicker, 2006: Effects of upper-level shear on the structure and maintenance of strong quasi-linear mesoscale convective systems. *J. Atmos. Sci.,* **63,** 1231–1252.

Cressman, G. P., 1959: An operational objective analysis system. *Mon. Wea. Rev.,* **87,** 367–374.

Doviak, R. J., P. S. Ray, R. G. Strauch, and L. J. Miller, 1976: Error estimation in wind fields derived from dual-Doppler radar measurement. *J. Appl. Meteor.,* **15,** 868–878.

Dowell, D. C., and H. B. Bluestein, 2002a: The 8 June 1995 McLean, Texas, storm. Part I: Observations of cyclic tornadogenesis. *Mon. Wea. Rev.,* **130,** 2626–2648.

——, and ——, 2002b: The 8 June 1995 McLean, Texas, storm. Part II: Cyclic tornado formation, maintenance, and dissipation. *Mon. Wea. Rev.,* **130,** 2649–2670.

Frame, J., P. Markowski, Y. Richardson, J. Straka, and J. Wurman, 2009: Polarimetric and dual-Doppler radar observations of the Lipscomb County, Texas, supercell thunderstorm on 23 May 2002. *Mon. Wea. Rev.,* **137,** 544–561.

Gao, J., M. Xue, A. Shapiro, and K. K. Droegemeier, 1999: A variational method for the analysis of three-dimensional wind fields from two Doppler radars. *Mon. Wea. Rev.,* **127,** 2128–2142.

Given, T., and P. S. Ray, 1994: Response of a two-dimensional dual-Doppler radar wind synthesis. *J. Atmos. Oceanic Technol.,* **11,** 239–255.

Jorgensen, D. P., and B. F. Smull, 1993: Mesovortex circulations seen by airborne Doppler radar within a bow-echo mesoscale convective system. *Bull. Amer. Meteor. Soc.,* **74,** 2146–2157.

Joss, J., and A. Waldvogel, 1970: Raindrop size distribution and Doppler velocities. Preprints, *14th Conf. on Radar Meteorology,* Tucson, AZ, Amer. Meteor. Soc., 153–156.

Kessinger, C. J., P. S. Ray, and C. E. Hane, 1987: The Oklahoma squall line of 19 May 1977. Part I: A multiple Doppler analysis of convective and stratiform structure. *J. Atmos. Sci.,* **44,** 2840–2865.

Knupp, K. R., 1996: Structure and evolution of a long-lived, microburst-producing storm. *Mon. Wea. Rev.,* **124,** 2785–2806.

Koch, S. E., M. desJardins, and P. J. Kocin, 1983: An interactive Barnes objective map analysis scheme for use with satellite and conventional data. *J. Climate Appl. Meteor.,* **22,** 1487–1503.

Lee, W.-C., R. E. Carbone, and R. M. Wakimoto, 1992: The evolution and structure of a ''bow-echo–microburst'' event. Part I: The microburst. *Mon. Wea. Rev.,* **120,** 2188–2210.

Majcen, M., P. Markowski, Y. Richardson, D. Dowell, and J. Wurman, 2008: Multipass objective analyses of Doppler radar data. *J. Atmos. Oceanic Technol.,* **25,** 1845–1858.

Mansell, E. R., C. L. Ziegler, and E. C. Bruning, 2010: Simulated electrification of a small thunderstorm with two-moment bulk microphysics. *J. Atmos. Sci.,* **67,** 171–194.

Markowski, P., and Coauthors, 2012: The pretornadic phase of the Goshen County, Wyoming, supercell of 5 June 2009

intercepted by VORTEX2. Part II: Intensification of low-level rotation. *Mon. Wea Rev.,* in press.

Marquis, J., Y. Richardson, J. Wurman, and P. Markowski, 2008: Single- and dual-Doppler analysis of a tornadic vortex and surrounding storm-scale flow in the Crowell, Texas, supercell of 30 April 2000. *Mon. Wea. Rev.,* **136,** 5017–5043.

Matejka, T., and D. L. Bartels, 1998: The accuracy of vertical air velocities from Doppler radar data. *Mon. Wea. Rev.,* **126,** 92–117.

O'Brien, J. J., 1970: Alternative solutions to the classical vertical velocity problem. *J. Appl. Meteor.,* **9,** 197–203.

Potvin, C. K., D. Betten, L. J. Wicker, K. L. Elmore, and M. I. Biggerstaff, 2012: 3DVAR vs. traditional dual-Doppler wind retrievals of a simulated supercell thunderstorm. *Mon. Wea. Rev.,* in press.

——, A. Shapiro, and M. Xue, 2012b: Impact of a vertical vorticity constraint in variational dual-Doppler wind analysis: Tests with real and simulated supercell data. *J. Atmos. Oceanic Technol.,* **29,** 32–49.

Ray, P. S., K. K. Wagner, K. W. Johnson, J. J. Stephens, W. C. Bumgarner, and E. A. Mueller, 1978: Triple-Doppler observations of a convective storm. *J. Appl. Meteor.,* **17,** 1201–1212.

——, C. L. Ziegler, W. Bumgarner, and R. J. Serafin, 1980: Single- and multiple-Doppler radar observations of tornadic storms. *Mon. Wea. Rev.,* **108,** 1607–1625.

Raymond, W. H., 1988: High-order low-pass implicit tangent filters for use in finite area calculations. *Mon. Wea. Rev.,* **116,** 2132–2141.

Shapiro, A., C. K. Potvin, and J. Gao, 2009: Use of a vertical vorticity equation in variational dual-Doppler wind analysis. *J. Atmos. Oceanic Technol.,* **26,** 2089–2106.

——, K. M. Willingham, and C. K. Potvin, 2010a: Spatially variable advection correction of radar data. Part I: Theoretical considerations. *J. Atmos. Sci.,* **67,** 3445–3456.

——, ——, and ——, 2010b: Spatially variable advection correction of radar data. Part II: Test results. *J. Atmos. Sci.,* **67,** 3457–3470.

Taylor, G. I., 1938: The spectrum of turbulence. *Proc. Roy. Soc. London,* **164A,** 476–490.

Trapp, R. J., and C. A. Doswell, 2000: Radar data objective analysis. *J. Atmos. Oceanic Technol.,* **17,** 105–120.

Wakimoto, R. M., C. Liu, and H. Cai, 1998: The Garden City, Kansas, storm during VORTEX 95. Part I: Overview of the storm's life cycle and mesocyclogenesis. *Mon. Wea. Rev.,* **126,** 372–392.

Weisman, M. L., and J. B. Klemp, 1982: The dependence of numerically simulated convective storms on vertical wind shear and buoyancy. *Mon. Wea. Rev.,* **110,** 504–520.

——, and ——, 1984: The structure and classification of numerically simulated convective storms in directionally varying wind shears. *Mon. Wea. Rev.,* **112,** 2479–2498.

Wicker, L. J., and W. C. Skamarock, 2002: Time-splitting methods for elastic models using forward time schemes. *Mon. Wea. Rev.,* **130,** 2088–2097.

Wood, V. T., R. A. Brown, and D. C. Dowell, 2009: Simulated WSR-88D velocity and reflectivity signatures of numerically modeled tornadoes. *J. Atmos. Oceanic Technol.,* **26,** 876–893.

Wurman, J., J. Straka, E. Rasmussen, M. Randall, and A. Zahrai, 1997: Design and deployment of a portable, pencil-beam, pulsed, 3-cm Doppler radar. *J. Atmos. Oceanic Technol.,* **14,** 1502–1512.

——, Y. Richardson, C. Alexander, S. Weygandt, and P. F. Zhang, 2007: Dual-Doppler analysis of winds and vorticity budget terms near a tornado. *Mon. Wea. Rev.,* **135,** 2392–2405.

Ziegler, C. L., 1985: Retrieval of thermal and microphysical variables in observed convective storms. Part 1: Model development and preliminary testing. *J. Atmos. Sci.,* **42,** 1487–1509.

——, E. N. Rasmussen, T. R. Shepherd, A. I. Watson, and J. M. Straka, 2001: The evolution of low-level rotation in the 29 May 1994 Newcastle–Graham, Texas, storm complex during VORTEX. *Mon. Wea. Rev.,* **129,** 1339–1368.